

A novel Reverberation mapping method for blazars

JUNHAO DENG ^{1,2} LIZHI LIU,^{1,2} YIFAN WANG ³ AND YUNGUO JIANG ^{1,2}

¹*Shandong Provincial Key Laboratory of Optical Astronomy and Solar-Terrestrial Environment, Institute of Space Sciences, Shandong University, Weihai, 264209, People's Republic of China*

²*School of Space Science and Technology, Shandong University, Weihai 264209, People's Republic of China*

³*College of Physics and Electronic Information, Dezhou University, Dezhou 253023, People's Republic of China*

ABSTRACT

The reverberation mapping (RM) is the most promising method to measure the mass of supermassive black hole in the center of active galaxy nuclei (AGNs). However, the dominant jet component hinders the application of RM method for blazars. In this work, we present a new algorithm to disentangle the contributions of the accretion disk and relativistic jet in blazars by analyzing the optical spectroscopic data. Applying this method to two flat-spectrum radio quasars, PKS 1510-089 and PKS 0736+017, we find that the H γ variability in PKS 1510-089 lags behind the disk by approximately 116 days, while the H β line exhibits a lag of about 52 days relative to the disk in PKS 0736+017. Based on these measured time lags, we estimate that the black hole masses are about $1.8 \times 10^8 M_{\odot}$ for PKS 1510-089 and about $7.0 \times 10^7 M_{\odot}$ for PKS 0736+017, respectively. This method paves the way to apply the RM method for blazars, and improves the understanding of disk and jet activities.

Keywords: Active galactic nuclei (16); Blazars (164); Supermassive black holes (1663)

1. INTRODUCTION

Active galactic nuclei (AGNs) are among the brightest objects in the Universe, and have a supermassive black hole (SMBH) at their centers. The accretion process of SMBH leads to distinct radiative structural components, including the accretion disk and the broad-line region (BLR). The BLR consists of high-velocity gas, which is mainly photoionized by the ultraviolet (UV) and optical photons from the accretion disk. The profile of the broad emission lines traces the kinematic and spatial distribution of the gas (C. M. Urry & P. Padovani 1995). The luminosity variation of the accretion disk will lead to the time-delay responses of the emission-lines (e.g., B. M. Peterson et al. 1992, 2002; K. T. Korista & M. R. Goad 2004; D. Park et al. 2012; A. J. Barth et al. 2015; C. Hu et al. 2015). This time delay can be measured by using methods such as the discrete correlation function (DCF, R. A. Edelson & J. H. Krolik 1988), the interpolated cross-correlation function (ICCF, B. M. Peterson et al. 1998), and the local cross-correlation function (LCCF, W. F. Welsh 1999) to estimate the size of the BLR. Assuming the virial motion of BLR gas, the mass of the SMBH can be estimated from the lag and the full width at half maximum (FWHM) of the broad emission lines, with the inclusion of a virial factor f that accounts for the geometry and kinematics of the BLR. This technique is known as reverberation mapping (RM, B. M. Peterson 1993).

However, it is difficult to apply the RM process to blazars, a special class of AGNs with their relativistic jet directed almost along the observer's line of sight. The jet emission normally is Doppler boosted, and highly variable. In the optical-UV band, the emission is composed of radiation from both the accretion disk and the jet (G. Ghisellini et al. 2010). Therefore, disentangling the varied disk and jet components is a key to measure the SMBH mass in blazars by using the RM process. Some previous studies have attempted to use the Non-Thermal Dominance (NTD) parameter to classify the jet-dominated and disk-dominated data for blazars (S. Pandey et al. 2022; A. Amador-Portes et al. 2024). It is assumed that when $\text{NTD} < 2$, the specific fluxes at 5100 Å is dominated by the accretion disk. This method relies on a relatively straightforward threshold-based criterion, which may limit its robustness. In other words, even when the NTD is below 2, variability from the jet may still contribute to the observed fluxes, potentially disturbing

the correlation analysis. Besides, the NTD less than 2 cases are unpredictable and mostly happen during quiescent states. These ingredients significantly intervene the application of the RM procedure for blazars.

In this paper, we present a approach to distinguish the contributions of the accretion disk and the jet, and pave a way for the application of RM for a subclass of blazars. Blazars with broad emission lines are classified as flat-spectrum radio quasars (FSRQs). According to the broad band spectral energy distribution (SED), FSRQs are typically categorized as the low-synchrotron-peaked blazars, with the peak frequency of the synchrotron bump lying below 10^{14} Hz (A. A. Abdo et al. 2010). Thus, in the optical observation window, the jet emission exhibits a power-law spectrum with negative spectral index in the $\log \nu F_\nu$ versus $\log \nu$ plot. The accretion disk, contributing the big blue bump (BBB) in the SED, usually peaks in the UV band and shows a positive spectral index in the optical window. Therefore, we can predict that the spectroscopic data is expected to show a spectral break when the disk and jet emissions differ by less than a magnitude. Thus, by quantitatively modeling the spectral break, we are able to disentangle the contributions from the accretion disk and the jet. In this work, we select PKS 1510-089 and PKS 0736+017 as case studies to explore the feasibility of this new approach, since both targets have the abundant publicly available spectroscopic data and evident spectral break. The structure of this paper is organized as follows. Section 2 details the data analysis and processing. Section 3 presents the results, and Section 4 offers discussion and conclusions.

2. DATA REDUCTION

All spectroscopic data used in this study are from the Steward Observatory⁴. These Data were obtained with the 2.3 m Bok Telescope on Kitt Peak and the 1.54 m Kuiper Telescope on Mount Bigelow in Arizona, using the SPOL spectropolarimeter (G. D. Schmidt et al. 1992). A 600 mm^{-1} grating provided a spectral range of 4000-7550 Å with a dispersion of 4 Å /pixel; depending on the slit width, the spectral resolution was typically 16–24 Å. Flux calibration followed the procedure described in P. S. Smith et al. (2009): spectra were first calibrated using sensitivity functions derived from spectrophotometric standard stars, and then re-scaled to match the synthetic V-band photometry for each night. The dataset employed in this work has previously been used in earlier studies (S. Pandey et al. 2022; A. Amador-Portes et al. 2024, 2025). From the public website of the Steward Observatory, we downloaded 371 spectra of PKS 1510-089 (observed between MJD 54,830 and 58,307), 130 spectra of PKS 0736+017 (observed between MJD 56,989 and 58,251). The Galactic interstellar extinction and reddening of all spectra were corrected by the procedure given in J. A. Cardelli et al. (1989), and $E(B - V)$ of sources refers to the NASA/IPAC Extragalactic Database⁵. The spectra spans a frequency range from approximately $10^{14.60}$ to $10^{14.88}$ Hz.

2.1. Spectral Break

The top-left and top-right panels of Figure 1 display spectra of PKS 0736+017 and PKS 1510-089 at three different flux levels. At the low-flux states, the spectra exhibit a concave shape in the plane of $\log \nu$ versus $\log \nu F_\nu$, namely a spectral break. This spectral break shifts, becomes less prominent and gradually disappears at the high-flux levels.

To illustrate the origin of the spectral break, we show the time-averaged broadband SEDs of PKS 1510-089 and PKS 0736+017, compiled from historical archival data downloaded from the Space Science Data Center⁶ (SSDC) in bottom panels of Figure 1. We reproduced the broadband SEDs using a one-zone leptonic model. Details of the model and its parameters are provided in Appendix A. Within the observing band, the total energy flux consists of two components, a red component and a blue component. The red component corresponds to the non-thermal synchrotron emission from the jet, while the blue component arises from thermal emission of the accretion disk.

In general, the variability of the jet is more significant than that of the accretion disk. When the target changes from a quiescent state to an active state, both the peak flux and frequency of the jet component increase (C.-Z. Wang & Y.-G. Jiang 2024; J.-T. Wang & Y.-G. Jiang 2025; J. Deng & Y. Jiang 2025). Consequently, the spectral break evident in low-flux states disappears in the high-flux states.

2.2. Emission Lines Fitting Scheme

In this section, we describe the method used to obtain the light curve of emission lines through the spectral fitting procedure. First of all, the observed spectroscopic data were shifted to the rest-frame wavelengths based on their redshifts. The redshift values used are $z = 0.361$ for PKS 1510-089 (E. M. Burbidge & T. D. Kinman 1966) and $z = 0.189$ for PKS 0736+017 (C. R. Lynds 1967).

⁴ <https://james.as.arizona.edu/~psmith/Fermi/>

⁵ <https://ned.ipac.caltech.edu/>

⁶ <https://tools.ssdc.asi.it/SED/>

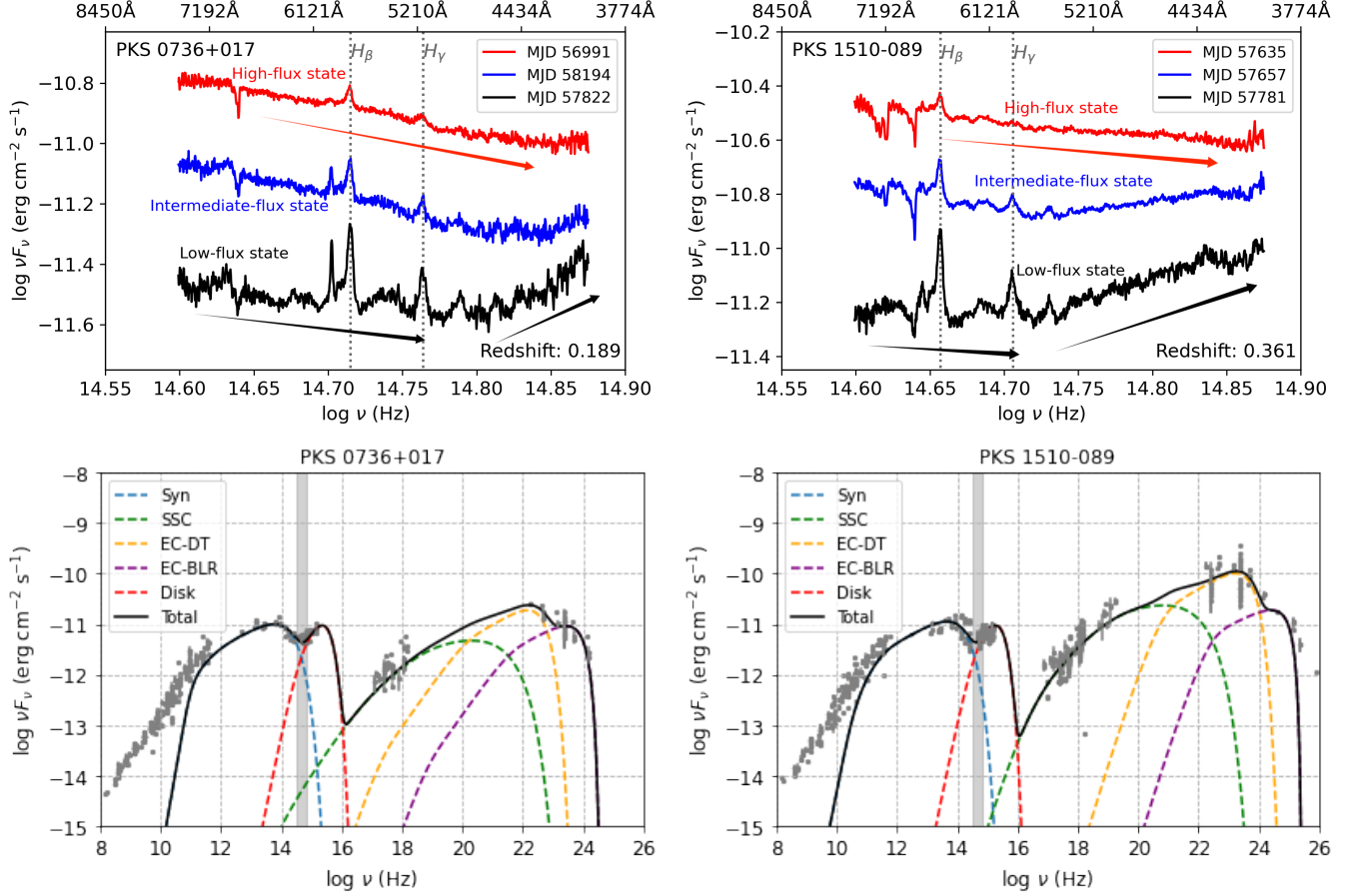


Figure 1. Top panels: Representative optical spectra of PKS 0736+017 (left) and PKS 1510-089 (right) in three different flux states. The arrows approximately mark the local spectral slope, serving as visual guides. Bottom panels: Broadband SEDs of PKS 0736+017 (left) and PKS 1510-089 (right), compiled from archival data and modeled by using the one-zone leptonic model (see Appendix A). The shaded gray regions mark the optical observation window. The overlap of jet and disk components confirms that both contribute to the observed optical emission.

For both targets, the H β and H γ broad lines are present within the optical window. For PKS 0736+017, we selected the H β line for analysis and extracted spectra from 4800 Å to 5050 Å, since the H β line is prominent than H γ . In the case of PKS 1510-089, there is strong telluric absorption features near 4861 Å. Thus, we chose to fit the H γ instead, using the spectra from 4250 Å to 4500 Å. The spectra at all epochs were stacked to produce the time-average spectra for each target, shown in Figure 2.

Then, we performed the spectral fitting on the time-averaged spectra, aiming to obtain the fixed Fe II and host galaxy components. The fitting model includes the Fe II emission template (T. A. Boroson & R. F. Green 1992), the host galaxy template (G. Bruzual & S. Charlot 2003), and a power-law spectrum representing the continuum. Although, in principle, the continuum including the emission of both jet and disk should not be fully described by a single power-law, such approximation serves as a reasonable substitute over the narrow wavelength ranges considered in our fitting. The emission lines are modeled by the Gaussian function. For PKS 0736+017, the fitting model includes the H β λ 4861, [O III] λ 4959, and [O III] λ 5007 emission lines. For PKS 1510-089, we considered H γ λ 4340, [O III] λ 4363, and He I λ 4471 in the fitting model. Both the Fe II and host galaxy templates are convolved with the Gaussian function to be scaled, broadened, and shifted. The host galaxy template for both targets was chosen to be the age of 11 Gyr and metallicity $Z = 0.05$. After incorporating all these components, we search the minimal χ^2 result using the Markov Chain Monte Carlo (MCMC) method. The fitting result of the stacked spectra are illustrated in Figure 2. In practice, after fitting, we found that the host galaxy contribution is negligible for both sources. This is because of their relatively high redshifts.

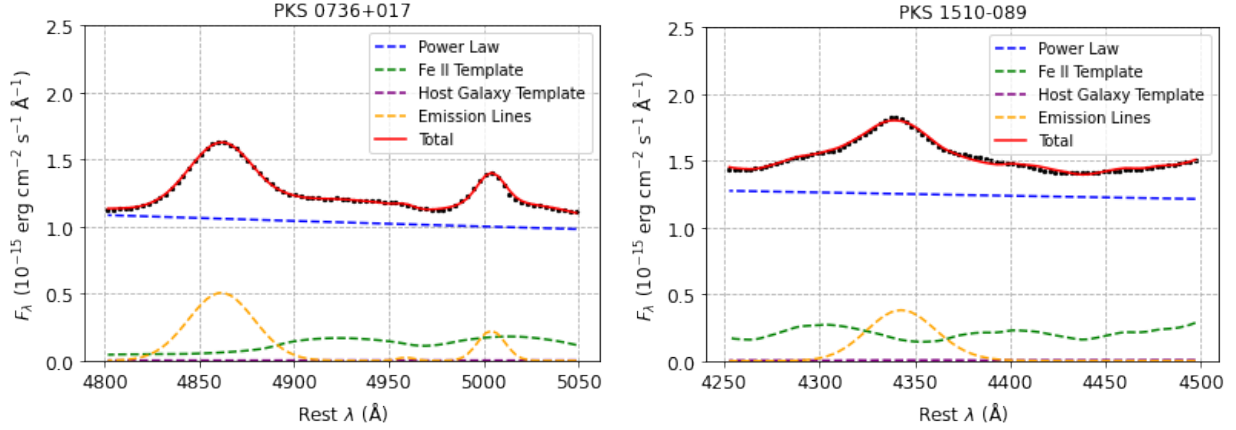


Figure 2. Multi-component spectral fitting of the average optical spectra for PKS 0736+017 (left) and PKS 1510-089 (right). The model consists of a power-law continuum (representing the combined jet and disk emission), an Fe II template, a host galaxy template, and multiple Gaussian profiles for the emission lines. For PKS 0736+017, the fit includes the H β λ 4861, [O III] λ 4959, and [O III] λ 5007 emission lines within the rest-frame wavelength range of 4800–5050 Å. For PKS 1510-089, due to strong telluric absorption near H β , the fitting is performed in the 4250–4500 Å range, including H γ λ 4340, [O III] λ 4363, and He I λ 4471 lines.

Adopting the fitted Fe II and host galaxy components as well as the convolving mode, we fit the spectra at each epoch with the same algorithm. Through the numerical integration of the Gaussian functions, we obtained the flux and FWHM of the emission lines. Finally, we collect all these fluxes to obtain the light curves of emission lines.

2.3. Disentangle the disk and jet

To disentangle the emission from the accretion disk and the jet, we employed a broader spectral range ($\log \nu$ [Hz] from 14.60 to 14.88) rather than the narrow range used in Section 2.2. The jet component was modeled with a power-law spectrum with a negative spectral index, while the accretion disk was modeled by the Shakura-Sunyaev model (N. I. Shakura & R. A. Sunyaev 1973). All disk parameters except the luminosity were fixed based on the fitting result of the broad band SED shown in bottom panels of Figure 1.

To reduce the complication of the fitting process, we first subtracted the contributions of the host galaxy and Fe II emission with parameters adopted from the time-averaged spectra in Section 2.2. Second, we excluded the spectral ranges containing prominent emission lines and atmospheric absorption. Specifically, we masked the 4800-4900 Å around H β λ 4861, the 4950-5050 Å around [O III] λ 5007, and the 4300-4400 Å around H γ λ 4340.

The spectra at different epochs may have different ratio of jet over disk components. Thus, we consider three fitting models, i.e., (1) only the jet, (2) only the disk, and (3) both the jet and the disk. For each case, we calculated the value of Akaike Information Criterion (AIC), which considers the trade-off between goodness of fit and model complexity. The lower value of AIC indicates a better result. In many cases, the case (3) gives the lowest AIC, suggesting that the jet and disk have comparable contributions, as shown in Figure 3. At high flux states, case (1) gives the lowest AIC, which indicates the dominance of jet component. However, across all observed spectra of PKS 1510-089 and PKS 0736+017, we did not find any epoch in which the case (2) yielded the lowest AIC. In addition, the jet-only model (case 1) provides the lowest AIC in 28% of the observations for PKS 1510-089, and in 22% of the observations for PKS 0736+017.

Finally, the fluxes of the disk and jet components within the observed frequency range were calculated via numerical integration. The light curves of emission lines, disk component, and jet component for two targets are plotted in Figure 4.

3. REVERBERATION MAPPING

In this work, we used the ICCF method (B. M. Peterson et al. 1998) for the correlation analysis between two light curves, following the same procedure as used in S. Pandey et al. (2022). Figure 5 present the results. It can be seen that for both blazars, the ICCF peaks correspond to negative lags, indicating that the variations of the accretion disk flux lead those of the broad emission lines. We computed the centroid lag (τ_c) for each source. For PKS 1510-089, we

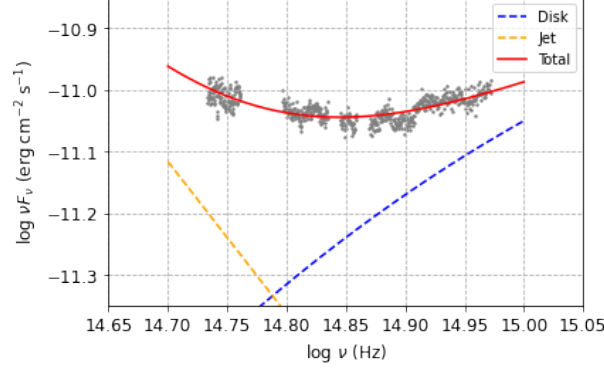


Figure 3. Spectral decomposition of PKS 1510-089 on MJD 57129, shown as a representative example to illustrate the disk–jet emission separation method. The gray points show the optical spectrum after removal of the host galaxy, Fe II emission, prominent emission lines, and atmospheric absorption features. The orange dashed line represents the power-law component corresponding to non-thermal jet emission, while the blue dashed line represents thermal emission from the accretion disk, modeled with the Shakura-Sunyaev model. The red solid line shows the total emission combining both components.

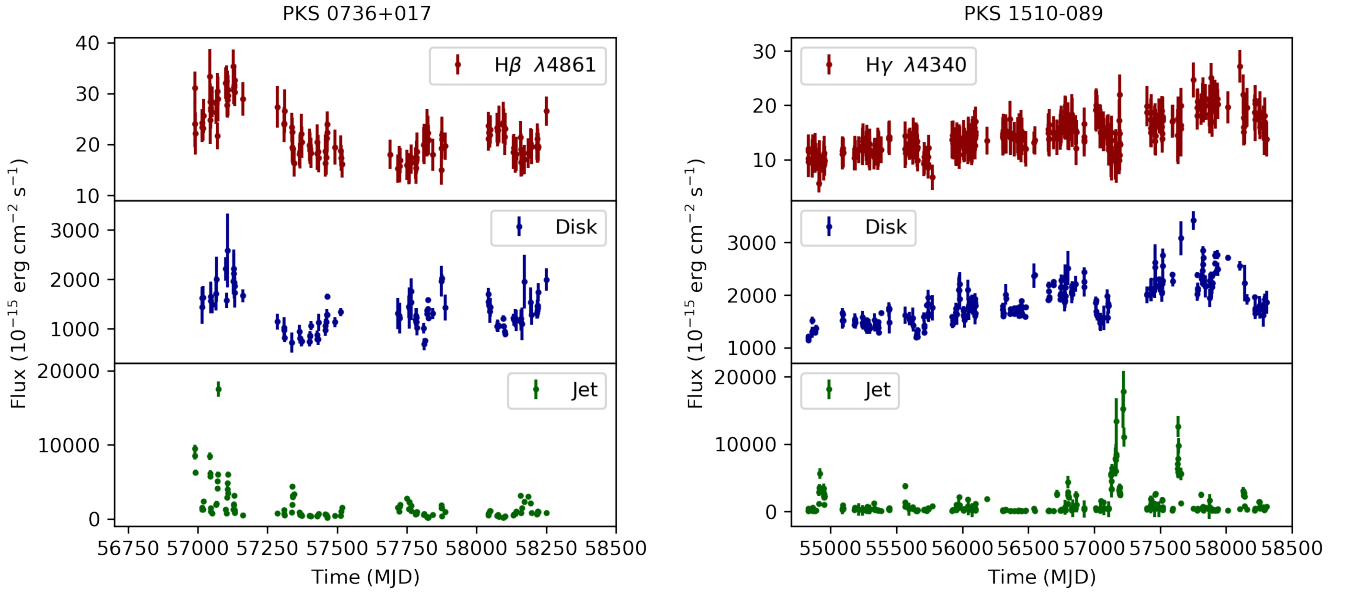


Figure 4. Light curves of broad emission line (red), accretion disk (blue), and the jet (green) for PKS 0736+017 (left) and PKS 1510-089 (right).

obtained $\tau_c = -115.9^{+38.3}_{-32.1}$ days. For PKS 0736+017, the corresponding values are $\tau_c = -52.2^{+32.2}_{-21.8}$ days. These results are consistent with expectations that, in most AGNs, the variability of broad emission lines typically lags behind that of the accretion disk continuum by several tens of days.

Using the measured time lags, we can estimate the black hole masses of both blazars. The black hole mass is calculated using the formula from B. M. Peterson et al. (2004):

$$M_{\text{BH}} = f \frac{R_{\text{BLR}} \Delta V^2}{G} = f \frac{c \tau_c \Delta V^2}{G} \quad (1)$$

where f , set to 1.12 (J.-H. Woo et al. 2015), is a dimensionless scale factor that depends on the kinematics and geometry of BLR gas clouds, c is the speed of light, $R_{\text{BLR}} = c \tau_c$ is the BLR size, G is the gravitational constant, and ΔV represents the velocity dispersion of the broad emission line, which is calculated according to the FWHM of the line. We average the FWHM at all epochs to obtain the mean FWHM. For PKS 1510-089, the mean FWHM of the $\text{H}\gamma$ line is 2693 km/s. For PKS 0736+017, the mean FWHM of the $\text{H}\beta$ line is 2470 km/s. Based on these values and

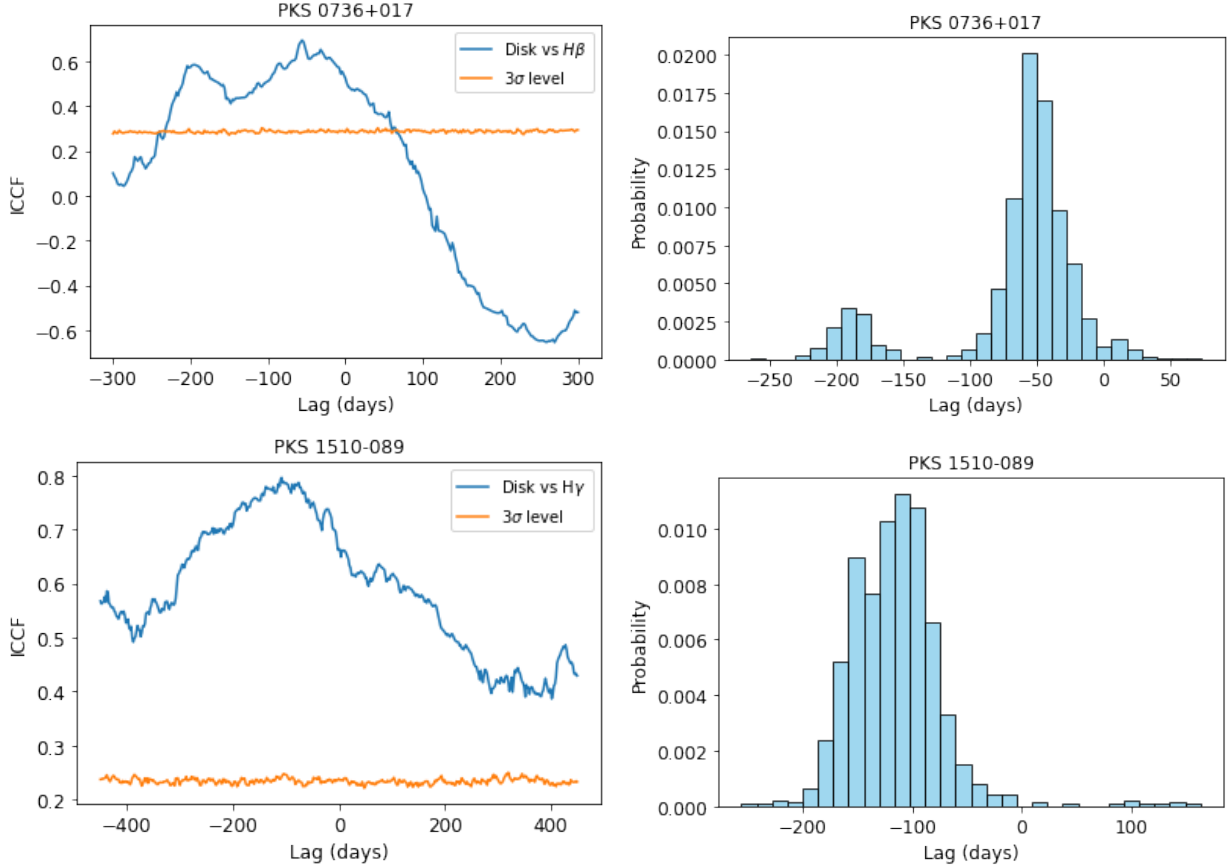


Figure 5. Top panels: The ICCF (left panel) and centroid probability distribution (right panel) between the accretion disk continuum and the H β emission line in PKS 0736+017. Bottom panels: The ICCF (left panel) and centroid probability distribution (right panel) between the accretion disk continuum and the H γ emission line in PKS 1510-089. The negative lag indicates that the former leads the latter.

the measured time lags, the estimated black hole masses are $1.8^{+0.5}_{-0.6} \times 10^8 M_{\odot}$ for PKS 1510-089 and $7.0^{+2.9}_{-4.3} \times 10^7 M_{\odot}$ for PKS 0736+017, respectively.

4. DISCUSSION AND CONCLUSION

Previous studies have made efforts to perform reverberation mapping on the blazars PKS 1510-089 and PKS 0736+017, both of which relied on the NTD parameter to separate disk and jet contributions. For PKS 1510-089, [A. Amador-Portes et al. \(2024\)](#) performed a correlation analysis between the H β line and the 5100 Å continuum after excluding data points with NTD > 2, and reported a time lag of about 80 days. This method works mainly because that the accretion disk in PKS 1510-089 is intrinsically bright, with only about 30% of the data points having NTD > 2. In contrast, for PKS 0736+017, [S. Pandey et al. \(2022\)](#) also calculated the NTD values and found that the average NTD is as high as 2.7. This indicates that the majority of the 5100 Å data points are jet-dominated. If all data points with NTD > 2 are excluded, more than half of the dataset would be removed, making it difficult to conduct a reliable correlation analysis. In addition, they performed the correlation analysis between the V-band and H β . They reported that the H β line was found to lag the V-band by approximately 60 days, and the ICCF peak was below 0.5. In our algorithm, the filtered data points with valid disk fluxes are 72% and 78% of the all measurements for PKS 1510-089 and PKS 0736+017, respectively. Thus, our algorithm discards fewer data compared to the NTD-based selection, thereby preserving more time series for correlation analysis. Also, the peaks of ICCF for both targets exceed 0.6 and the 3σ line, which also produce significant results than the previous RM methods for blazars.

One valid condition of our method is that the targets show spectral break at the optical window. For blazars such as 3C 454.3 and 3C 279, where the optical–UV continuum is almost entirely jet-dominated and the thermal “big blue

bump” component is virtually undetectable (V. S. Paliya et al. 2021), our method does not work. The fraction of the valid targets for the blazar RM will be answered for a sample work in the future.

In summary, we proposed a novel approach to perform reverberation mapping of blazars by disentangling the disk and jet components through reproducing the spectral break identified in the $\log \nu$ versus $\log \nu F_\nu$ plane. Applying this method to PKS 1510-089 and PKS 0736+017, we successfully obtained the light curves of the accretion disk and emission lines, and obtained the fiducial lags between them. The measured time lags of $115.9^{+38.3}_{-32.1}$ days for PKS 1510-089 and $52.2^{+32.2}_{-21.8}$ days for PKS 0736+017 allowed us to estimate the black hole masses to be $1.8^{+0.5}_{-0.6} \times 10^8 M_\odot$ and $7.0^{+2.9}_{-4.3} \times 10^7 M_\odot$, respectively. Compared to traditional NTD-based selection methods, our approach retains more data and provides more significant lag estimation. Our method paves a way for the mass measurements of black holes for specific jet-dominated AGNs.

ACKNOWLEDGMENTS

The data underlying this article were accessed from the Steward Observatory data base with the following link: <http://james.as.arizona.edu/~psmith/Fermi/> (see, P. S. Smith et al. 2009). This work has been funded by the National Natural Science Foundation of China under grant No. U2031102, and the Shandong Provincial Natural Science Foundation under grant No. ZR2023MA036.

Software: agnpy (C. Nigro et al. 2022)

APPENDIX

A. MULTI-WAVELENGTH SED MODEL

We employed the traditional one-zone leptonic model to reproduce the broadband SEDs presented in bottom panels of Figure 1. This model, widely used for blazars, assumes a homogeneous spherical emission region of radius R , embedded in a magnetic field B . The region moves relativistically along the jet with a velocity $v = \beta c$, corresponding to a bulk Lorentz factor $\Gamma = (1 - \beta^2)^{-1/2}$. A Doppler factor $\delta = [\Gamma(1 - \beta \cos \theta)]^{-1} \approx \Gamma$ is adopted, assuming a small viewing angle $\theta < 1/\Gamma$, typical for blazar jets. The radiative processes include the synchrotron emission, the synchrotron self-Compton (SSC), and external Compton (EC) process. The calculation of spectrum refers to G. B. Rybicki & A. P. Lightman (1979).

Following S.-J. Kang et al. (2016); R. Khatoon et al. (2022); J. Deng & Y. Jiang (2023), we assumed that the electron energy distribution in the emission zone follows a broken power-law, characterized by spectral indices p_1 and p_2 below and above the broken Lorentz factor γ_b , respectively. The distribution is expressed as:

$$N(\gamma) = \begin{cases} N_0 \gamma^{-p_1} & \gamma_{\min} \leq \gamma \leq \gamma_b, \\ N_0 \gamma_b^{p_2 - p_1} \gamma^{-p_2} & \gamma_b < \gamma \leq \gamma_{\max} \end{cases} \quad (\text{A1})$$

where γ_{\min} and γ_{\max} are the minimal and maximal electron Lorentz factors, and N_0 is the normalized particle number density.

For the EC emission, the seed photons are assumed to originate from both the BLR and the DT. Following R. Khatoon et al. (2022); J. Deng & Y. Jiang (2024), we model the photon fields from the BLR and DT as single-temperature blackbody spectra with temperatures of $T_{\text{BLR}} = 4.2 \times 10^4$ K and $T_{\text{DT}} = 10^3$ K, respectively. Their photon energy densities, u_{BLR} and u_{DT} , are treated as free parameters.

We model the accretion disk as a geometrically thin, optically thick Shakura–Sunyaev disk (N. I. Shakura & R. A. Sunyaev 1973), using the agnpy⁷ Python package (C. Nigro et al. 2022). The inner and outer disk radii are set to the default values, $R_{\text{in}} = 6 R_g$ and $R_{\text{out}} = 200 R_g$, where R_g is the gravitational radius. The radiative efficiency is also fixed $\eta = 1/12$, representing the fraction of accreted mass energy converted into radiation. As a result, the accretion disk component only has two free parameters: the black hole mass (M_{BH}) and the disk luminosity (L_{disk}).

⁷ <https://agnpy.readthedocs.io/en/latest/index.html>

To reproduce the broadband SED, a total of thirteen parameters are required: N_0 , γ_{\min} , γ_b , γ_{\max} , p_1 , p_2 , B , R , δ , u_{DT} , u_{BLR} , L_{disk} , and M_{BH} . Given the complexity of the parameter space, applying rigorous optimization methods such as MCMC would be computationally expensive and difficult to converge. Thus, the model parameters were tested within feasible values to fit the SEDs by eye estimation such as A. Roy et al. (2021). Finally, for PKS 1510-089, the adopted model parameters are as follows: $N_0 = 398 \text{ cm}^{-3}$, $\gamma_{\min} = 300$, $\gamma_b = 500$, $\gamma_{\max} = 10000$, $p_1 = 1.3$, $p_2 = 2.3$, $B = 0.016 \text{ G}$, $R = 0.01 \text{ pc}$, $\delta = 32$, $u_{\text{DT}} = 9 \times 10^{-5} \text{ erg cm}^{-3}$, $u_{\text{BLR}} = 3 \times 10^{-5} \text{ erg cm}^{-3}$, $L_{\text{disk}} = 4 \times 10^{45} \text{ erg s}^{-1}$, $M_{\text{BH}} = 6 \times 10^8 M_{\odot}$. For PKS 0736+017, the adopted model parameters are as follows: $N_0 = 251 \text{ cm}^{-3}$, $\gamma_{\min} = 10$, $\gamma_b = 300$, $\gamma_{\max} = 4600$, $p_1 = 1.3$, $p_2 = 2.3$, $B = 0.25 \text{ G}$, $R = 0.01 \text{ pc}$, $\delta = 11$, $u_{\text{DT}} = 4 \times 10^{-3} \text{ erg cm}^{-3}$, $u_{\text{BLR}} = 3 \times 10^{-3} \text{ erg cm}^{-3}$, $L_{\text{disk}} = 4 \times 10^{45} \text{ erg s}^{-1}$, $M_{\text{BH}} = 4 \times 10^8 M_{\odot}$.

REFERENCES

- Abdo, A. A., Ackermann, M., Ajello, M., et al. 2010, *ApJ*, 715, 429, doi: [10.1088/0004-637X/715/1/429](https://doi.org/10.1088/0004-637X/715/1/429)
- Amador-Portes, A., Chavushyan, V., Patiño-Álvarez, V. M., & Ramón-Valdés, J. 2025, *ApJ*, 979, 227, doi: [10.3847/1538-4357/ada38b](https://doi.org/10.3847/1538-4357/ada38b)
- Amador-Portes, A., García-Pérez, A., Chavushyan, V., & Patiño-Álvarez, V. M. 2024, *ApJ*, 977, 178, doi: [10.3847/1538-4357/ad8ddd](https://doi.org/10.3847/1538-4357/ad8ddd)
- Barth, A. J., Bennert, V. N., Canalizo, G., et al. 2015, *ApJS*, 217, 26, doi: [10.1088/0067-0049/217/2/26](https://doi.org/10.1088/0067-0049/217/2/26)
- Borison, T. A., & Green, R. F. 1992, *ApJS*, 80, 109, doi: [10.1086/191661](https://doi.org/10.1086/191661)
- Bruzual, G., & Charlot, S. 2003, *MNRAS*, 344, 1000, doi: [10.1046/j.1365-8711.2003.06897.x](https://doi.org/10.1046/j.1365-8711.2003.06897.x)
- Burbidge, E. M., & Kinman, T. D. 1966, *ApJ*, 145, 654, doi: [10.1086/148808](https://doi.org/10.1086/148808)
- Cardelli, J. A., Clayton, G. C., & Mathis, J. S. 1989, *ApJ*, 345, 245, doi: [10.1086/167900](https://doi.org/10.1086/167900)
- Deng, J., & Jiang, Y. 2023, *MNRAS*, 521, 6210, doi: [10.1093/mnras/stad821](https://doi.org/10.1093/mnras/stad821)
- Deng, J., & Jiang, Y. 2024, *PASP*, 136, 124101, doi: [10.1088/1538-3873/ad95bc](https://doi.org/10.1088/1538-3873/ad95bc)
- Deng, J., & Jiang, Y. 2025, *ApJ*, 983, 128, doi: [10.3847/1538-4357/adc106](https://doi.org/10.3847/1538-4357/adc106)
- Edelson, R. A., & Krolik, J. H. 1988, *ApJ*, 333, 646, doi: [10.1086/166773](https://doi.org/10.1086/166773)
- Ghisellini, G., Tavecchio, F., Foschini, L., et al. 2010, *MNRAS*, 402, 497, doi: [10.1111/j.1365-2966.2009.15898.x](https://doi.org/10.1111/j.1365-2966.2009.15898.x)
- Hu, C., Du, P., Lu, K.-X., et al. 2015, *ApJ*, 804, 138, doi: [10.1088/0004-637X/804/2/138](https://doi.org/10.1088/0004-637X/804/2/138)
- Kang, S.-J., Zheng, Y.-G., Wu, Q., & Chen, L. 2016, *MNRAS*, 461, 1862, doi: [10.1093/mnras/stw1312](https://doi.org/10.1093/mnras/stw1312)
- Khatoon, R., Prince, R., Shah, Z., Sahayanathan, S., & Gogoi, R. 2022, *MNRAS*, 513, 611, doi: [10.1093/mnras/stac892](https://doi.org/10.1093/mnras/stac892)
- Korista, K. T., & Goad, M. R. 2004, *ApJ*, 606, 749, doi: [10.1086/383193](https://doi.org/10.1086/383193)
- Lynds, C. R. 1967, *ApJ*, 147, 837, doi: [10.1086/149068](https://doi.org/10.1086/149068)
- Nigro, C., Sitarek, J., Gliwny, P., et al. 2022, *A&A*, 660, A18, doi: [10.1051/0004-6361/202142000](https://doi.org/10.1051/0004-6361/202142000)
- Paliya, V. S., Böttcher, M., Gurwell, M., & Stalin, C. S. 2021, *ApJS*, 257, 37, doi: [10.3847/1538-4365/ac365d](https://doi.org/10.3847/1538-4365/ac365d)
- Pandey, S., Rakshit, S., Woo, J.-H., & Stalin, C. S. 2022, *MNRAS*, 516, 2671, doi: [10.1093/mnras/stac2418](https://doi.org/10.1093/mnras/stac2418)
- Park, D., Woo, J.-H., Treu, T., et al. 2012, *ApJ*, 747, 30, doi: [10.1088/0004-637X/747/1/30](https://doi.org/10.1088/0004-637X/747/1/30)
- Peterson, B. M. 1993, *PASP*, 105, 247, doi: [10.1086/133140](https://doi.org/10.1086/133140)
- Peterson, B. M., Wanders, I., Bertram, R., et al. 1998, *ApJ*, 501, 82, doi: [10.1086/305813](https://doi.org/10.1086/305813)
- Peterson, B. M., Alloin, D., Axon, D., et al. 1992, *ApJ*, 392, 470, doi: [10.1086/171447](https://doi.org/10.1086/171447)
- Peterson, B. M., Berlind, P., Bertram, R., et al. 2002, *ApJ*, 581, 197, doi: [10.1086/344197](https://doi.org/10.1086/344197)
- Peterson, B. M., Ferrarese, L., Gilbert, K. M., et al. 2004, *ApJ*, 613, 682, doi: [10.1086/423269](https://doi.org/10.1086/423269)
- Roy, A., Patel, S. R., Sarkar, A., Chatterjee, A., & Chitnis, V. R. 2021, *MNRAS*, 504, 1103, doi: [10.1093/mnras/stab975](https://doi.org/10.1093/mnras/stab975)
- Rybicki, G. B., & Lightman, A. P. 1979, *Radiative processes in astrophysics*
- Schmidt, G. D., Stockman, H. S., & Smith, P. S. 1992, *ApJL*, 398, L57, doi: [10.1086/186576](https://doi.org/10.1086/186576)
- Shakura, N. I., & Sunyaev, R. A. 1973, *A&A*, 24, 337
- Smith, P. S., Montiel, E., Rightley, S., et al. 2009, *arXiv e-prints*, arXiv:0912.3621, doi: [10.48550/arXiv.0912.3621](https://doi.org/10.48550/arXiv.0912.3621)
- Urry, C. M., & Padovani, P. 1995, *PASP*, 107, 803, doi: [10.1086/133630](https://doi.org/10.1086/133630)
- Wang, C.-Z., & Jiang, Y.-G. 2024, *ApJ*, 966, 65, doi: [10.3847/1538-4357/ad2fc7](https://doi.org/10.3847/1538-4357/ad2fc7)
- Wang, J.-T., & Jiang, Y.-G. 2025, *MNRAS*, 536, 1251, doi: [10.1093/mnras/stae2609](https://doi.org/10.1093/mnras/stae2609)
- Welsh, W. F. 1999, *PASP*, 111, 1347, doi: [10.1086/316457](https://doi.org/10.1086/316457)
- Woo, J.-H., Yoon, Y., Park, S., Park, D., & Kim, S. C. 2015, *ApJ*, 801, 38, doi: [10.1088/0004-637X/801/1/38](https://doi.org/10.1088/0004-637X/801/1/38)